Ultrasound Energy Harvesting System for Deep Implanted-Medical-Devices (IMDs)

Francesco Mazzilli*, Prakash E. Thoppay†, Vincent Praplan*, and Catherine Dehollain*
*Ecole Polytechnique Fédérale de Lausanne, RFIC group, Lausanne, 1015, Switzerland
†Marvell, Etoy, 1163, Switzerland

***Abstract*—It is desirable in active medical implants to derive energy from external sources to charge a rechargeable battery. In this paper we have developed a novel system to transfer energy via ultrasound to a deep implanted medical device. Hence, an external base station is designed to transmitt energy and a 64-channel high-voltage driver is proposed for a spherical transducer array. Moreover, a shunt-C class-E power amplifier (PA) is employed as core element for the driver, showing a drain efficiency (DE) of 71% and a power added efficiency (PAE) of 57% including gate-driver switching loss. In addition, a cascaded of two low-drop-out (LDO) regulators is used within the implanted device to reduce rectifier ripple and to set the charge voltage for the micro-energy cell to 4.1 V. The LDOs are implemented in a CMOS 0.18 μm high-voltage (HV) technology and measurement along with simulated results are reported.**

***Index Terms*—CMOS, energy harvesting, implanted medical device, power management, healthcare, sensor networks.**

I. Introduction

Requirements for active implanted medical devices (IMDs) deeply introduced into the human body are ruled by the implant size (1-3 cm^3) and by the type of coupling used to transmitt energy [1]. RF and magnetic induced coupling are heavily attenuated in water, whereas ultrasound is a valid option to overcome this limit despite the complexity to choose the carrier frequency [2].

The selection of the wavelength (λ) for delivering energy is guided by the transducer design. For instance a spherical array transducer enables to focus the ultrasound (US) beam without beamforming electronics. However, to track the implant when it goes out-of-focus, each array element needs a power amplifer (PA) to shape the acoustic field. A good candidate in energy transmission is the class-E power amplifier with a theoretical power efficiency up to 100 % [3].

However, it is more challenging the choice of the CMOS technology used for energy conversion in the implant. To avoid oxide breakdown, HV transistors are employed as the input available voltage can be expected to vary from few millivolts to tens of volt. In medical ultrasound as the carrier frequency is setted around 1 MHz, two series LDO are used to further improve supply noise rejection at low frequency.

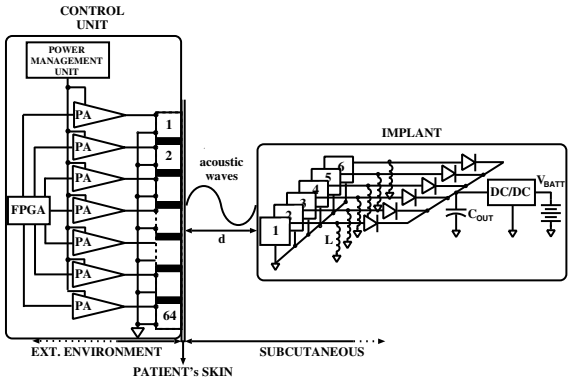

Fig. 1. Ultrasound energy harvesting system chain.

The paper discusses the class-E PA design as well as power management details within the implanted device. In Section II the ultrasound energy harvesting system is proposed. In Section III an analysis and tuning methodology to calibrate 64-PA is described. In Section IV the LDO architecture to improve power-supply-rejection-ratio (PSRR) is shown. Lastly, the conclusions are given in section V.

II. Ultrasound Wireless Power Transfer

Figure 1 shows the block diagram of the US wireless power transfer (WPT) system, a 64-elements spherical transducer array is used for the control unit (CU) while a 6-elements flat transducer array is employed for the implant. The natural focus of the spherical array, point of maximum intensity, is located at distance (d) of 11 cm and the focal area measured at -6 dB is 2 x 5 mm^2. The implanted transducer has a total active area of 5 x 10 mm^2 (SA_{tot}) and the active area per element of the array is 5 x 1 mm^2 (SA). Hence rectifiers should be connected to add the current yielded by the elements of the array since the focal area is smaller than SA_{tot},. To boost the rectifier output voltage an off-chip shunt inductor (L) is used to resonate with the tranducer and the rectifier imaginary part.

For US-WPT a governing equation is nonexisting to estimate the power link budget as function of frequency selection and transducer design by considering all the chain which includes the external PA, the attenuation

in the body and the load of the implant. Hence, the following approach is used to design the power amplifier and to determine the input voltage range at the DC-to-DC converter. A narrowband model is assumed for the piezoelectric (PZT) tranducers and the implant is always presumed at the spatial peak of maximum intensity.

III. Shunt-C Class-E Power Amplifier

Figure 2 shows the shunt-C class-E power amplifier along with the driving amplifer and a transducer equivalent model represented by a parallel branch constituted by the capacitor (C_t) in series with the resistor (R_t).

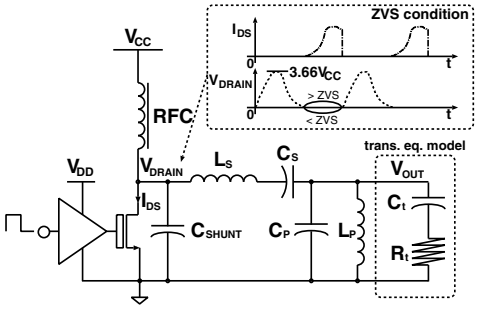

Fig. 2. Shunt-C class-E power amplifier with transducer equivalent model.

The parallel inductor L_P resonates with the transducer at 1 MHz, the series capacitor C_S prevents any DC feedthrough, the parallel capacitors C_{SHUNT} and C_P helps to achieve zero voltage switching (ZVS). The series inductor L_S increases the power amplifier efficiency since the AC current through L_P decreases and as consequence the iron loss decreases.

A. Tuning Methodology

Design equations have been developed for the class-E power amplifier [4], henceforth in this section a tuning strategy is proposed. The shunt-C class-E power amplifier is designed with Advanced Design System (ADS) and an average value for R_t and C_t is considered. 64-PA are fabricated on standard substrate FR4 due to the low-frequency requirement.

Figure 3 shows the tuning methodology adopted to calibrate 64-PAs, two main loops can be distinguished to set respectively the output voltage (V_{OUT}) of the PA to the desired voltage (V_{GOAL}) and to achieve ZVS for best efficiency. To set the value for the capacitors the magnitude $|V_{OUT} - V_{GOAL}|$ is compared with ΔV_1 or ΔV_2. The initial conditions $\Delta V_{1,0}$, $\Delta V_{2,0}$ for ΔV_1, ΔV_2 are chosen within the range $[0.1 \div 1]$ V and their values also dermine the final maximum distance between V_{OUT} and V_{GOAL}.

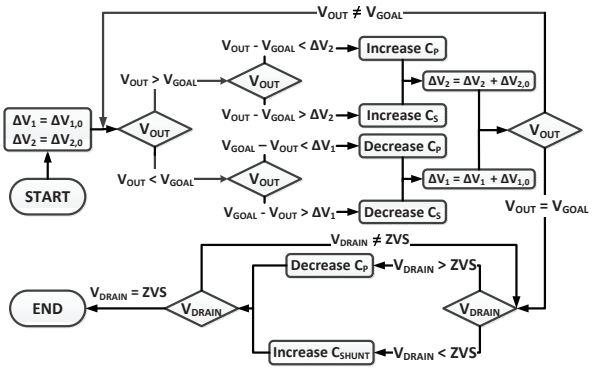

Fig. 3. Tuning methodology for the calibration of multiple shunt-C class-E power amplifer.

B. Measurements

Figure 4 represents the histogram of the number of amplifiers versus the measured output voltage before and after using the tuning methodology. A 37 % of the number of PAs reach $V_{OUT} = V_{GOAL} = 19$ Vpeak, while the remaining 63 % present a shift only of ± 1 V from V_{GOAL}.

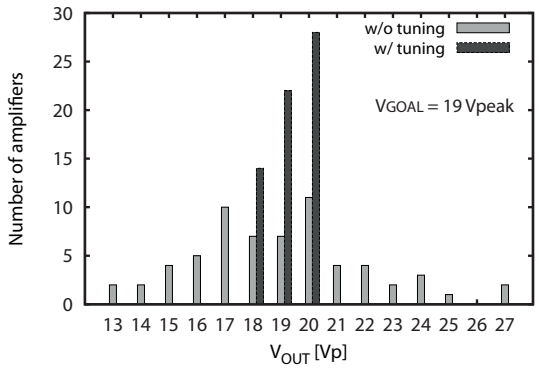

Fig. 4. Number of amplifiers versus the output voltage w/ and w/o tuning.

To evaluate the efficiency of the shunt-C class-E power amplifier a prototype is realized and the transducer is replaced by its series lumped equivalent model ($R_t = 120\Omega$, $X_t = -j290\Omega$). Figure 5 shows the prototype efficiency versus the DC power supply (V_{CC}) while V_{DD} is kept constant. Drain efficiency (eqn. 1a) and power added efficiency (eqn. 1b) are measured for the power amplifier.

$$DE = \frac{P_{OUT,RF}}{P_{V_{CC}}} \tag{1a}$$

$$PAE = \frac{P_{OUT,RF} - P_{DYN}}{P_{V_{CC}}} \tag{1b}$$

Where $P_{OUT,RF}$ is the delivered power to R_t, $P_{V_{CC}}$ is the DC power and P_{DYN} is the dynamic power consumed by the driver during the charge/discharge of the gate-to-source and gate-to-drain capacitances of the power MOS. According to Figure 5, the ripple on DE is less that 10% on all the scale of V_{CC} whereas the ripple on PAE is less that 10% for V_{CC} larger than 3 V.

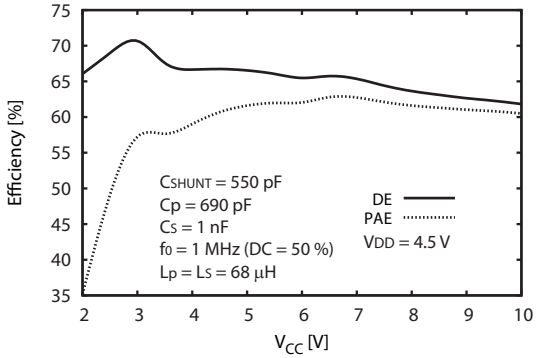

Fig. 5. Efficiency of the tuned shunt-C class-E power amplifier.

The 64-PAs are able to deliver an acoustic intensity (I_{ac}) in water of 23 W/cm^2 at 11 cm with $P_{V_{CC},tot}$ equals to 8 W and $P_{OUT,RF_{tot}}$ equals to 5.4 W. The acoustic intensity is measured via the hydrophone HGL-0200 (ONDA) which average sensitivity is -264.3 dB re. $1V/\mu Pa$ and its associated amplifier. The US-WPT link efficiency can be expressed as the ratio between the received electrical power P_{load} and the delivered electrical power $P_{OUT,RF_{tot}}$ [2], [5]:

$$\eta_{link} = \frac{P_{load}}{P_{OUT,RF_{tot}}} = \frac{I_{ac} \times SA \times \eta_{ae}}{P_{OUT,RF_{tot}}} \quad (2)$$

Where $\eta_{ae} = 50\%$ is the acousto-electric efficiency for one element of the implanted tranducer array. Assuming a conjugate load matching at each element of the implanted tranducer ends, the maximum theoretical US-WPT link efficiency is 10.6%.

IV. Two Stage LDO

Figure 6 depicts the linear DC-to-DC converter that sets the charging voltage of the battery (see Figure 1). A current mirror OTA (OTA1) and a basic OTA (OTA2) are designed in a CMOS 0.18 μm HV technology to enhance PSRR. The rectifier output voltage (V_{rec}) is regulated to $V_{OUT1} =$ 4.2 V and $V_{BATT} = 4.1$ V. To evaluate PSRR with respect to V_{rec}, the reference voltage (V_{ref}) is provided externally and it is set to 1.2 V.

The micro-energy cell is represented by its Thevenin equivalent model with an equivalent capacitance of 277 mF (C_{BATT}), a cell equivalent series resistance of 180 Ω (ESR) and a self-discharge resistor (R_{self}) of 10 MΩ representing the battery leakage.

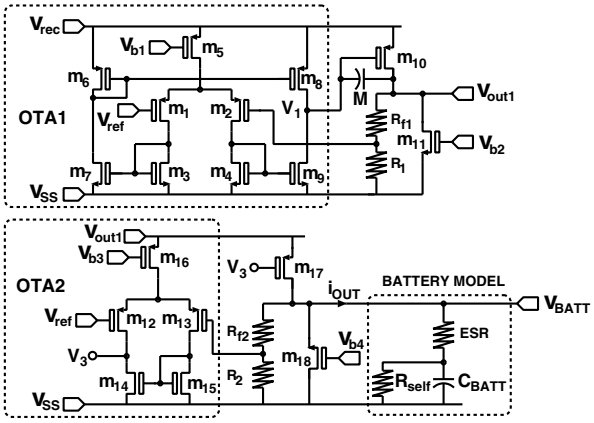

Fig. 6. Linear DC-to-DC converter to improve PSRR.

A. PSRR Analysis

A methodology to analyze PSRR is proposed in [6] by mean of control-theory. Figure 7 represents an equivalent network of the two-series LDO to analyse PSRR at low frequency. Hence, V_{OUT1} and V_{BATT} can be expressed as follows:

$$V_{OUT1} = \frac{A_1 A_2}{1 + \beta_1 A_1 A_2} V_{ref} + \frac{A_2 (1 - A_{p1}) + A_{p2}}{1 + \beta_1 A_1 A_2} V_{rec} \quad (3a)$$

$$V_{BATT} = \frac{A_3 A_4}{1 + \beta_2 A_3 A_4} V_{ref} + \frac{A_4 (1 - A_{p3}) + A_{p4}}{1 + \beta_2 A_3 A_4} V_{OUT1} \quad (3b)$$

Where the attenuation factors are defined as $\beta_1 = \frac{R_1}{R_1 + R_{f1}}$ and $\beta_2 = \frac{R_2}{R_2 + R_{f2}}$. The supply gains are written as $A_{p1} = V_1/V_{rec}$, $A_{p2} = V_{OUT1}/V_{rec}$, $A_{p3} = V_3/V_{OUT1}$ and $A_{p4} = V_{BATT}/V_{OUT1}$. So, assuming $\beta_1 A_1 A_2 \gg 1$ and $\beta_2 A_3 A_4 \gg 1$, equations 3 can be rearragend as:

$$V_{OUT1} \approx \frac{V_{ref}}{\beta_1} + \frac{V_{rec}}{\beta_1} \frac{1}{PSRR_{LDO_1}} \quad (4a)$$

$$V_{BATT} \approx \frac{V_{ref}}{\beta_2} + \frac{V_{OUT1}}{\beta_2} \frac{1}{PSRR_{LDO_2}} \quad (4b)$$

Where $\frac{1}{PSRR_{LDO_1}} = \frac{1}{A_1} + \frac{1}{A_1 PSRR_2} + \frac{1}{PSRR_1}$ and $\frac{1}{PSRR_{LDO_2}} = \frac{1}{A_3} + \frac{1}{A_3 PSRR_4} + \frac{1}{PSRR_3}$. The parameters $PSRR_i$ are defined by $PSRR_1 = -\frac{A_1}{A_{p1}}$, $PSRR_2 = \frac{A_2}{A_{p2}}$, $PSRR_3 = -\frac{A_3}{A_{p3}}$ and $PSRR_4 = \frac{A_4}{A_{p4}}$. By replacing equation 4a into equation 4b, V_{BATT} can be expressed as follows:

$$V_{BATT} = \frac{1}{\beta_2} \left[\left(1 + \frac{1}{\beta_1 PSRR_{LDO_2}} \right) V_{ref} + \left(\frac{1}{PSRR_{LDO_1} PSRR_{LDO_2}} \right) \frac{V_{rec}}{\beta_1} \right] \quad (5)$$

At low frequency any variation in V_{rec} is further suppressed at V_{BATT} by using two LDOs in series as shown by the term $(PSRR_{LDO_1} \times PSRR_{LDO_2})^{-1}$.

B. Experimental Results

PSRR of the proposed LDO is measured using the methodology proposed in [7]. At low frequency PSRR

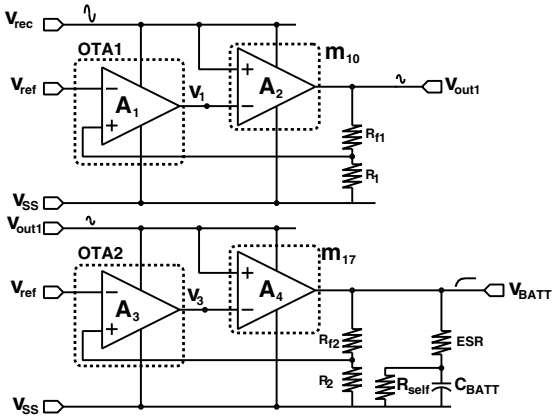

Fig. 7. Equivalent network of the linear DC-to-DC converter to improve PSRR.

measured at V_{BATT} is 10 dB above PSRR measured at V_{OUT1} (Figure 8(a)), while at high frequency both PSRRs dropped down to few dBs (Figure 8(b)). To compensate for the very low frequency pole introduced by the micro-cell battery and to improve PSRR at high frequency, a parallel bypass capacitor with low ESR can be added (Figure 8(b)).

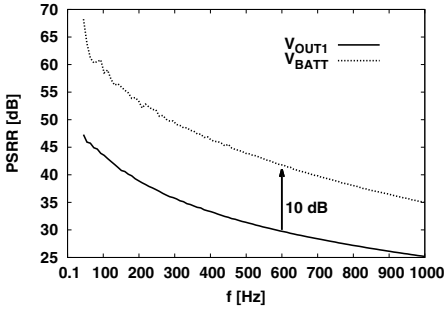

(a)

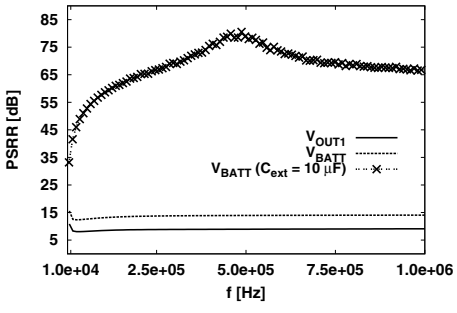

(b)

Fig. 8. Measured PSRR: (a) at low frequency [50 Hz : 1 kHz] and (b) at high frequency [10 kHz : 1 MHz].

Table I is a summary of the measured performance of the proposed LDO. Measured results are very close to simulated results (typical case), the variation is due to a shift in the pmos threshold voltage from $-1.4\ V$ (typical) to $-1.2\ V$ as reported by the process control monitor (PCM) characterization report of the foundry.

TABLE I
SUMMARY OF LDO SPECIFICATIONS AND PERFORMANCE

Parameter	
Input voltage (V)	$0 \div 9$ (V_{rec})
Load current (mA)	10 (i_{OUT})
Output voltage (V)	4.1 ± 0.05 (V_{BATT})
Battery capacity (μAh)	300 [8]
Drop voltage (mV)	200 (= V_{rec}-V_{BATT})
Ground current (μA)	210
Load regulation @ V_{OUT1} (mV/mA)	0.66 (simulated 0.6)
Line regulation $\frac{\Delta V_{OUT1}}{\Delta V_{rec}}$ (mV/V)	2.2 (simulated 0.8)
Load regulation @ V_{BATT} (mV/mA)	4.7 (simulated 1.6)
Line regulation $\frac{\Delta V_{BATT}}{\Delta V_{rec}}$ (mV/V)	0.08 (simulated 0.03)

V. CONCLUSION

A novel system to transfer energy via ultrasound to deep implanted medical devices has been proposed. The driving electronic for the external transducers showed a DE up to 71% for $V_{CC} = 3$ V and it was capable of delivering $I_{ac} = 23\ W/cm^2$ at 11 cm by leading to a theoretical $\eta_{link} = 10.6\%$. Moreover, to recharge a micro-battery in the implant, a linear dropout regulator was fabricated in a CMOS 0.18 μm HV technology. The LDO was successfully tested and measured along with simulated results were reported.

ACKNOWLEDGMENT

The research leading to these results has received funding from the European Community's Seventh Framework Programme (FP7/2007-2013) under grant agreement n. 224009. The authors thank IMASONIC that has provided the transducers and INSERM for his support during acoustic field measurements.

REFERENCES

[1] Xiaojuan Wei and Jing Liu. Power sources and electrical recharging strategies for implantable medical devices. *Frontiers of Energy and Power Engineering in China*, 2:1–13, 2008. 10.1007/s11708-008-0016-3.

[2] A. Denisov and E. Yeatman. Ultrasonic vs. inductive power delivery for miniature biomedical implants. In *Body Sensor Networks (BSN), 2010 International Conference on*, pages 84 –89, june 2010.

[3] P. Reynaert and M. Steyaert. *RF Power Amplifiers for Mobile Communications*. New York:Springer, 2006.

[4] M. Acar, A.J. Annema, and B. Nauta. Analytical design equations for class-e power amplifiers. *Circuits and Systems I: Regular Papers, IEEE Transactions on*, 54(12):2706 –2717, dec. 2007.

[5] Mazzilli F. et al. In-vitro platform to study ultrasound as source for wireless energy transfer and communication for implanted medical devices. In *EMBC 2010*, pages 3751 –3754, sept. 2010.

[6] M.S.J. Steyaert and W.M.C. Sansen. Power supply rejection ratio in operational transconductance amplifiers. *Circuits and Systems, IEEE Transactions on*, 37(9):1077 –1084, sep 1990.

[7] Texas Instrument. Ldo psrr measurement simplified: Slaa414, 2009.

[8] Infinity Power Solutions. http://www.infinitepowersolutions.com.